Journal of ELECTRONIC MATERIALS, Vol. 49, No. 1, 2020
https://doi.org/10.1007/s11664-019-07618-4

Mechanical Reliability of Photovoltaic Cells under Cyclic Thermal Loading

DIPALI SONAWANE,[1] PRAVEEN C. RAMAMURTHY,[1] and PRAVEEN KUMAR [1,2]

1.—Department of Materials Engineering, Indian Institute of Science, Bangalore 560012, India.
2.—e-mail: praveenk@iisc.ac.in

Metallic coatings placed on solar cell should retain their structural integrity over the life-span of the devices in order to ensure their reliable functioning. One critical component of such a life-assessment exercise is based on their response to the cyclic thermal stresses generated due to the temperature fluctuation, which is inevitable during regular operation of a solar cell and the difference in the thermal expansion coefficients of metal coatings and Si. Here, we have studied the impact of accelerated thermal cycling on the integrity of the semiconductor–metal layer in a commercial monocrystalline Si based photovoltaic solar cell comprising Ag finger-lining and Al backside coating. We observed that, compared to Si-Ag interface, the Al-Si interface was significantly weaker, wherein cracks easily nucleated and grew during thermal cycling between − 40°C and 90°C. The experimental results were augmented with finite element method (FEM), including extended-FEM (XFEM), simulations using geometry based on the actual microstructure of various metal-Si interfaces in the solar cell module. FEM-based simulations suggest excessive stress concentration at the interface of Al-Si eutectic-Al layers due to the irregular wavy nature of this interface. XFEM results indicate the critical role of the interfacial adhesion strength and roughness of the eutectic-Al interface on the crack growth and its propagation path. Based on the obtained results, a discussion on the fabrication of solar cell modules resistant to thermal stress induced structural damage is presented.

Key words: Fracture, metal-Si interface, Si based solar cells, thermal cycling, XFEM

INTRODUCTION

In recent years, photovoltaic (PV) energy has emerged as an important and affordable source of renewable energy. According to the International Energy Agency Photovoltaic Power Systems Programme (IEA PVPS) 2019 report, the global PV market has reached approximately 500 GW installed capacity, with an additional capacity of 50 GW added annually.[1] Considering the high financial and environmental costs involved in fabrication of PV modules and their field installation, it is important to ensure reliable operation of these modules over long periods for cost effective energy generation. In practice, a Si-based PV cell is essentially an ensemble of different class of materials, for example, it comprises a Si p–n junction that works as the “engine” of the PV solar cell module responsible for converting solar energy into electrical energy, metallic front and back coatings that act as electron collectors and electrodes, and polymer and glass based protective encapsulation. In particular, the following three major types of metal coatings are used in a typical PV solar cell module:

(Received April 29, 2019; accepted September 4, 2019; published online September 18, 2019)

(i) thin and narrow metal lines, often called fingers, that collect electrons on the top surface of a cell, (ii) slightly wider and thicker metal stripes, often called busbars, on the top surface of a cell for electric contact formation with adjacent cells, and (iii) a relatively thicker continuous planar layer at the back of the Si that enables the back-surface field (BSF) in PV cells and also acts as the backside electrode. In most of the commercial PV modules, Ag-rich glass frits and Al coatings are used as fingers and BSF-cum-backside electrode, respectively. In addition, the PV solar cell module is laminated with a transparent and complaint protecting polymer layer. In addition to the challenges associated with joining different class of materials for efficient power generation, large thermal stresses are generated in the solar cell system during operation due to thermal variations associated with the day-night and seasonal changes. It should be noted that the coefficient of thermal expansion (CTE) of the adjoining materials in a solar cell are widely different, e.g., CTE of Al, Ag and Si are 23.1×10^{-6}, 18.9×10^{-6} and 2.6×10^{-6}/°C, and hence a cyclic variation of 20°C, which is likely to occur during a day-night cycle, may generate a cyclic stress of ~ 40 MPa if a simple uniaxial loading condition is assumed. Such high cyclic stresses may induce significant fatigue loading, inducing deleterious effects on the structural integrity of various metal-Si interfaces. Hence, it is critical to examine the effect of thermal cycling induced cyclic thermal stress on the structural integrity of solar cell modules in the long term.

A few studies investigating the reliability of solar cells have focused on their structural integrity. A few studies[2,3] tested solar cell laminate using 3-point and 4-point loadings to understand the role of the microstructure of different components of the solar cell on its structural integrity and reported that metal layers had only minor effects on the stress distribution and stiffness of the solar cell.[3] An interesting study providing an overview of the failure modes in solar cells mentioned that the mechanical loads due to the snow and the wind as well as vibrations or thermo-mechanical stresses not only nucleate micro-cracks in the active layer of the device, but can also enhance the manufacturing defects, leading to debonding of the front metal contact.[4] In a comprehensive review on the degradation of PV solar cell modules, Nadiaye et al.[5] discussed various power degradation modes often observed at the macroscopic level, such as corrosion and discoloration of the encapsulant, delamination of the protecting glass and the polymer layers, and breakage and cracking of the glass.[6] Interestingly, temperature and humidity were reported to be the dominant factors responsible for almost all degradation modes.[5] However, the degradation modes reported in these studies were mainly based on the feedback or in-field observation of the solar modules over extended periods, and only limited number of investigations have used accelerated testing methods. Wohlegmuth et al.[7] and Skoczel et al.[8] employed accelerated testing protocols and, interestingly, reported only corrosion and delamination of the protecting layers, respectively, as the degradation mode. Bosco et al.[9] quantified the minimum adhesion energy values required to avoid delamination at the interfaces of the solar cell module laminates and suggested that adhesion properties of ethylene–vinyl acetate (EVA) and back sheet polymer layers are critical parameters for accessing the structural reliability of solar cells. However, the literature lacks a specific study that has rigorously investigated the degradation at the microstructure level, e.g., at the Si-metal interface, of solar cell components.

The finite element method (FEM) has been extensively applied to assess the thermo-mechanical behavior of complete PV laminates and the interconnect between two PV cells (including all front and back polymer/glass layers) under either thermal cycling or mechanical loading conditions. In one of such studies,[10] it was reported that the thickness of the glass controlled the overall thermo-mechanical behavior of the laminate, and the Cu interconnecting ribbons could readily crack due to the mechanical damage in the modules. Similarly, the critical role of the pre-stress (or residual stress) induced in the PV modules during assembly in determining the structural integrity of the modules was also confirmed using FEM.[11,12] Nevertheless, a study, whether experimental or numerical, focusing on understanding the role of microstructural features of the Si-metal interfaces in generating the stresses inside solar cell modules under thermal cycling conditions and eventually their effect on the structural integrity of the solar cell module is currently not available. Accordingly, here we perform accelerated thermal cycling tests on Si solar cells and study the role of the microstructure of the Si-Ag and the Al-Si interfaces on its mechanical failure by carefully observing the sample at pre-identified locations before and after thermal cycling. We have also used FEM, including extended-FEM (XFEM), to understand the effects of the microstructure of the Si-metal interface on the stress field established during thermal cycling and the strength of the interface on crack nucleation, crack growth and propagation path. Our results conclusively show that a smooth Si-metal interface, especially Al-Si interface, with high adhesion strength will slow the crack nucleation and growth by minimizing the stress field, and hence would improve the long-term reliability of a Si-based solar cell.

DETAILS OF EXPERIMENTS AND NUMERICAL ANALYSIS

Experimental Procedure

A commercial polymer laminated monocrystalline Si-solar cell was used in this study, and the

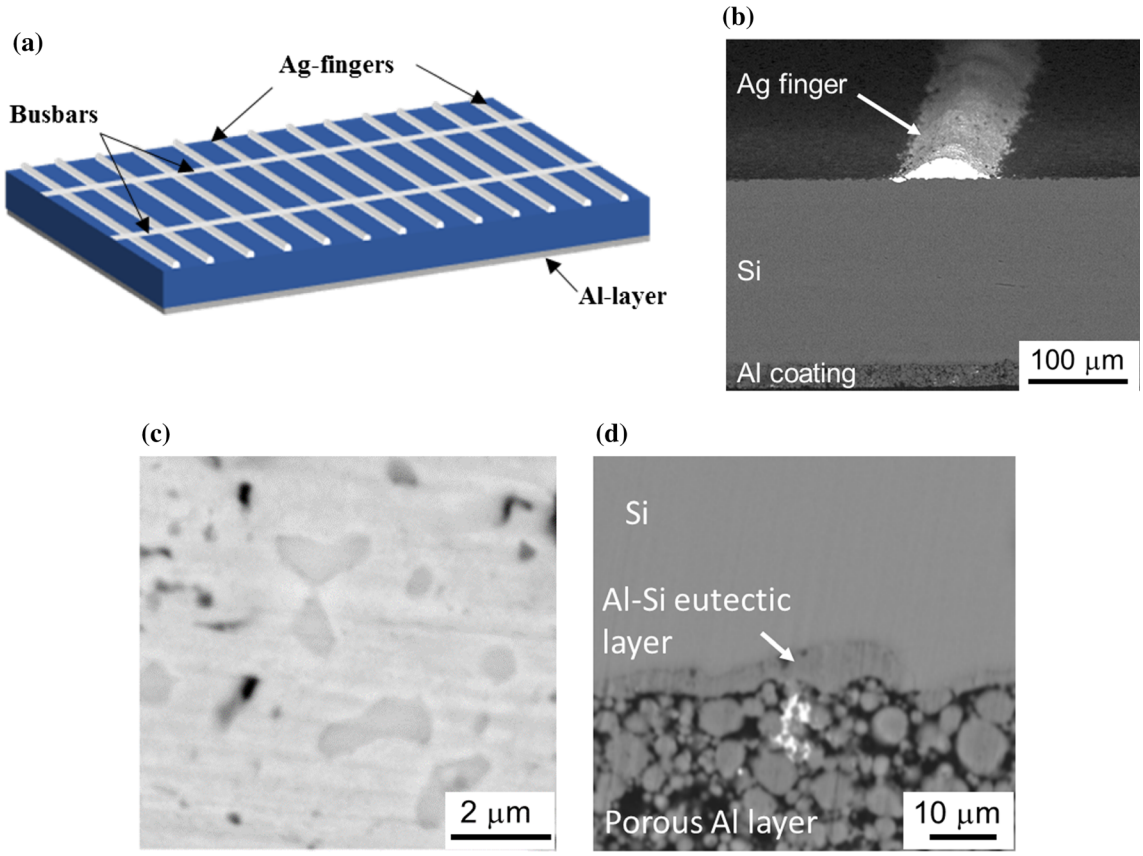

Fig. 1. (a) A 3D schematic of the commercial monocrystalline Si solar cell used in this study and scanning electron micrographs showing the (b) cross-sectional view of a solar cell coupons, (c) microstructure of the Ag finger at high magnification and (d) microstructure of the Al coating, along with the Al-Si interface. The continuous layer between the porous Al layer and Si was non-porous Al-Si eutectic layer.

microstructural details are shown in Fig. 1. Ag fingers comprising a mixture of different binding and adhesive materials were deposited in the line geometry (see Fig. 1b and c). As shown in Fig. 1b, the cross-section of the Ag finger was akin to a chordal-section of a right-angle cylinder, with a maximum thickness of $\sim$ 35–37 μm. Also, Fig. 1c shows random distribution of multiple phases, including pores, inside the Ag finger. A $\sim$ 25 μm thick planar coating of porous Al layer comprising spherical particles and appropriate binding constituents were sinter-deposited on the backside of the Si to form BSF layer and backside electrode. During firing process, a 3–4 μm thick Al-Si eutectic layer comprising 12–14% Si forms in between Si and Al.*[1] Since the thickness of the Si layer was 175 μm, thicknesses of the Ag finger and Al backside coating were significant enough to affect stresses deep inside the Si also during thermal cycling.

For fabricating small sized samples for testing and microstructural observation, a commercial solar cell panel was cut into small coupons comprising only a few fingers on the top layer using a low-speed diamond saw. For minimizing cutting induced damage in the sample, the cutting speed was maintained at an extremely low value and adequate coolant-lubricant was used. Subsequently, all sides of the cut sample coupons were metallographically polished up to 50 nm colloidal silica and observed under a scanning electron microscope (SEM) to verify if the prepared samples were mechanically undamaged prior to performing thermal cycling tests. More than 10 such samples were tested in this study for statistical purposes. In addition, locations of the observed regions were properly identified so that the same locations could be unambiguously tracked after a test to easily understand the effect of thermal cycling on the microstructure and the structural integrity (e.g., crack nucleation and growth).

In this study, the standard set by the International Electrotechnical Commission (IEC) for testing solar cell modules under accelerated conditions, namely IEC 61215, was employed, wherein the samples were thermally cycled between $-$ 40 and 90°C with a ramp-rate of 100°C/h. Figure 2 shows the temperature profile applied during thermal cycling. An environmental chamber with programmable temperature control was used to carry out the thermal cycling tests. The actual temperature of the sample was measured by placing a

*This was also confirmed through electron probe micro-analysis (EPMA) performed on the samples tested in this study.

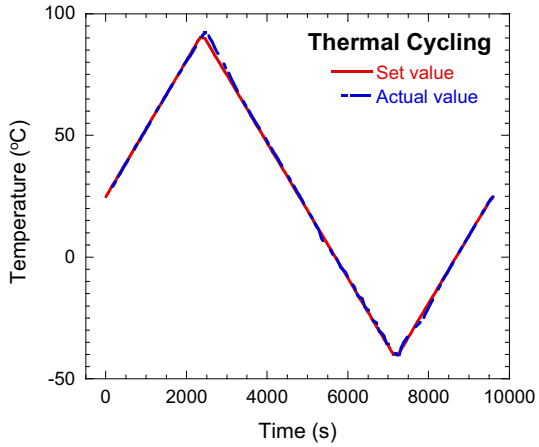

Fig. 2. Set and actual temperature profile during accelerated thermal excursion of solar cell samples. The actual temperature was measured using a thermocouple attached to the sample, whereas the set value in the figure corresponds to the programmed or desired temperature profile.

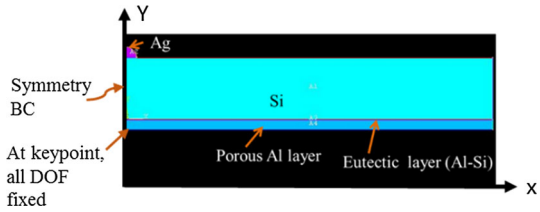

Fig. 3. Geometry and boundary conditions used during FEA of a solar cell sample. Here, BC and DOF represent boundary condition and degree of freedom, respectively.

thermocouple in contact with the sample. In a few tests the ramp-rate for heating and cooling was deliberately increased to $\sim$ 230°C/h to study the role of heating–cooling rate, which is akin the strain rate effect, on the structural integrity of the solar cells.

Procedure for Finite Element Method

2-D transient finite element (FE) simulation was performed using ANSYS®, a commercial software, for investigating effects of thermal cycling on the distribution of stress and strain fields in the solar cell samples. Figure 3 shows an example geometry used for performing FEM study. For better comparison between the experimental observations and FEM, simulations were performed by applying the cyclic temperature profile used in the experiments (see Fig. 2) as a periodic function type of boundary condition in ANSYS®. Relevant materials properties used in FEM were taken from references[2,3] and are listed in Table I. It should be noted that Si was assumed to be an isotropic elastic material, whereas various metal layers were modeled as bi-linear isotropic elasto-plastic materials. Eight-node quadrilateral elements (Plane183 in ANSYS® terminology) with generalized plane strain formulation were used to discretize the geometry; this type of element is capable of handling thermo-mechanical loading. Mesh insensitivity analysis was performed by gradually varying the mesh size from coarse to fine and evaluating the effect of mesh size on the value of the highest stress generated in the solar cell model. A mesh size that showed a convergence of $< 0.15\%$ for the highest stress value with a further reduction in the mesh size by 70% was used. As shown in Fig. 3, boundary conditions consistent with the experimental test conditions were applied during FE analysis. To reduce computational complexity, symmetric boundary condition was applied wherever possible.

In addition to the simple geometry shown in Fig. 3 wherein all material layers were assumed to be uniformly thick with perfectly flat interface, FEM study was also performed using a geometry based on the microstructure of the actual sample (see Fig. 1) for a better representation of the experiments. Here, a SEM micrograph, as shown in Fig. 4a, was considered for understanding stress–strain distributions near the Al-Si interface (which, as it will be discussed later, was more prone to failure). To avoid mesh convergence issues porous Al layer was considered uniform monolithic layer without any pores. Once the representative SEM micrograph was selected for performing FE simulations, it was firstly converted into a binary image using Image-J software (see Fig. 4b for an example for such a conversion for the micrograph shown in Fig. 4a). Subsequently, the pixels of the binary images were converted into x–y coordinates using a program written in MATLAB, which were then imported into ANSYS® as "Keypoints" for creating the geometry. Figure 4c show the geometry created using the imported pixel coordinates for the SEM micrograph shown in Fig. 4a. The acute similarity between the SEM micrograph and the FE geometry clearly confirms the efficacy of the procedure adopted for preparing the geometry used in the FEM study. Figure 4d shows the discretized finite element model. Other details related to the materials properties, the element formulations and the imposed boundary conditions used to perform these microstructurally sensitive FE simulations were kept the same as described in the context of Fig. 3.

Procedure for Extended Finite Element Analysis

2-D XFEM based quasi-static elastic simulations were performed using ABAQUS®, a commercial FEM software, to gain qualitative insights into effect of thermal cycling on the crack nucleation and propagation, as often observed in the experiments, near Al-Si interface, which, as it will be shown later, was more susceptible to fracture. In practice, XFEM was used to parametrically study effects of the strength and the geometry of the interface (e.g. smooth versus irregular wavy interface) on the failure during thermal cycling. Figure 5a shows an example geometry having irregular wavy Al-Si

Table I. Materials properties used in FE simulations. The properties were taken from the references [2, 3]

Material	Young's modulus, E (GPa)	Poisson's ratio (ν)	Yield strength, σ_{YS} (MPa)	Tangent Modulus (MPa)	CTE, α ($\times 10^{-6}$/°C)
Si	131	0.28	–	–	2.6
Ag finger	34	0.37	44	300	19
Al-Si eutectic layer	72	0.3	55	700	23
Al (porous layer)	32	0.3	39.5	60	23

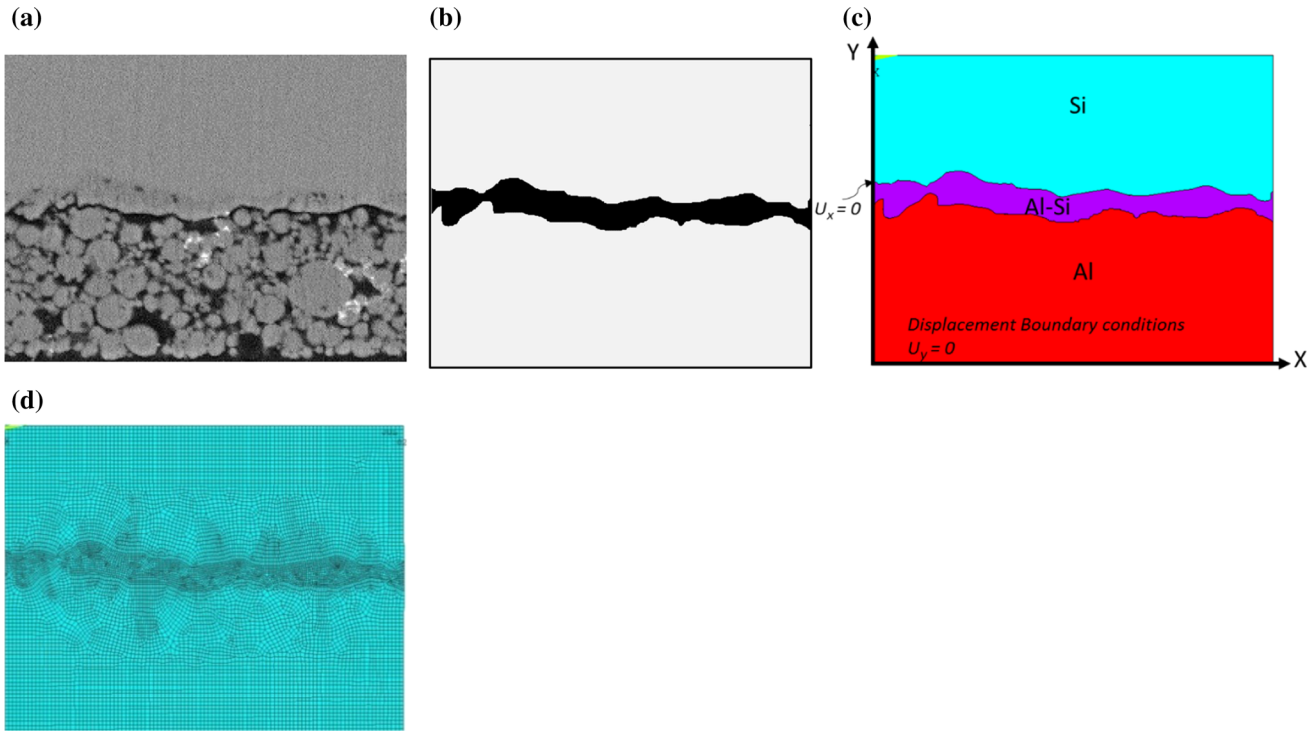

Fig. 4. (a) SEM micrograph showing region of solar cell near Al-Si interface, (b) corresponding binary image created using Image-J software, (c) geometry created in ANSYS® using imported pixel coordinates, along with applied displacement boundary conditions, and (d) the discretized geometry.

interface that was used to study the crack growth. The eutectic layer formed in between Si and Al layer was considered as a separate material region having a finite thickness. Both eutectic and Al layers were defined as the crack domain, wherein the initial crack was located near the interface between Al-Si eutectic and Al layers. As shown in Fig. 5b, XFEM model was discretized using linear quadrilateral elements. A cohesive segment approach was used in XFEM for damage modeling criteria, wherein crack nucleation occurred when the value of the maximum principal stress at the center of the enriched elements (used to define crack) exceeded a certain value. Hence, crack nucleation could not occur at the sharp interface in the XFEM models. In addition, the fracture energy-based traction separation criterion was used for crack growth analysis. The values of the different interface properties used are listed in the Table II. As shown in Table II, effect of the interface strength on the crack propagation was captured by varying the fracture strength. Since the goal of this study was to qualitatively understand the role of the interfacial strength on fracture, the values of interface fracture strength were arbitrary selected to be somewhat near to the Al properties to start with and varied until the crack started to propagate in a sample. The respective properties of Si and Al layers were taken as the values reported for bulk monolithic samples (see Table II). To understand the effect of interface geometry on the crack propagation, the extreme condition of perfectly smooth interface was also studied.

RESULTS AND DISCUSSIONS

Effect of Thermal Cycling on Structural Integrity of Solar Cell

Interestingly, as shown in Fig. 6a, a crack was observed near the Al-Si interface just after the first thermal cycle. Although the crack appears to be

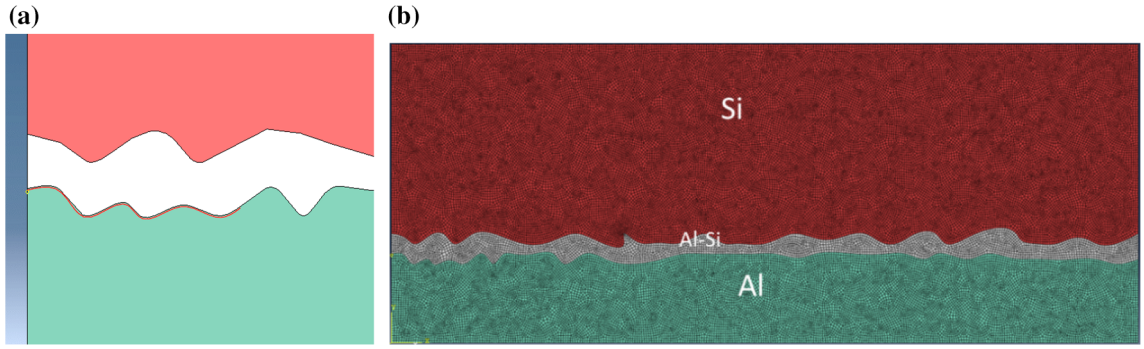

Fig. 5. Modeling the crack nucleation and growth in a region near Al-Si interface using XFEM: (a) geometry of a model with irregular wavy interface and (b) corresponding discretized geometry. Here, the top, middle and the bottom regions are Si, Al-Si eutectic and Al layers, respectively. In (a), the initial crack was already defined, as shown by the red colored curve at the interface between Al (green region) and Al-Si eutectic (white color) layers (Color figure online).

Table II. Materials properties used in the XFEM-based simulations

Relevant properties	Material	Model 1	Model 2	Young's modulus, E (GPa)	Poisson's ratio (ν)
Isotropic elastic material model	Al	Fracture strength: 150 MPa Fracture energy: 25 N/m CTE, $\alpha = 23 \times 10^{-6}$/°C	Fracture strength: 10 MPa Fracture energy: 2.5 N/m CTE, $\alpha = 23 \times 10^{-6}$/°C	32	0.3
	Al-Si eutectic	CTE, $\alpha = 20 \times 10^{-6}$/°C	CTE, $\alpha = 20 \times 10^{-6}$/°C	72	0.3
	Si	CTE, $\alpha = 2.6 \times 10^{-6}$/°C	CTE, $\alpha = 2.6 \times 10^{-6}$/°C	131	0.28

initiated at the (right) edge of the Si, it kinked away from the Si layer towards the porous Al layer and grew by almost 1 mm along the Al-Si interface during the first cycle itself. As shown in Fig. 6b, when the sample was exposed to further 99 thermal cycles, this crack did not deflect back into the brittle Si layer and continued to grow along the interface between the Al-Si eutectic and porous Al layers. Interestingly, as shown in Fig. 6c, delamination was mostly (≥ 70% of all 10 tested samples) observed at the interface between Al-Si eutectic and the Al layers. It should be noted that, nucleation of crack was never observed at the interface of Si and eutectic layer.

On the other hand, as shown in Fig. 7, the region of the solar cell near the Ag-Si interface was considerably less susceptible of cracking or delamination, as compared to the Al-Si interface. Only a few disjoint microcracks nucleated at this interface even after 70 thermal cycles. However, when the thermal cycling was performed using high ramp rates, then, as shown in Fig. 8, both Al-Si and Ag-Si interfaces delaminated completely after 10 (to 20) cycles. Interestingly, cracks were also observed inside Si layer under these harsh thermal cycling conditions. Nevertheless, the first instance of the delamination was still observed at the Al-Si interface under the harsh thermal cycling condition. Hence, a comparison of Figs. 6, 7 and 8 clearly reveals the important role of the strain rate (i.e., temperature ramp rate) on the structural integrity of solar cells.

In summary, Figs. 6, 7 and 8 readily reveal that the Al-Si interface was more susceptible to crack nucleation and growth, and hence delamination in these solar cells. This observed weakness of the Al-Si interface may be attributed to the high porosity of the Al layer and the irregular wavy nature of the interface between Al-Si eutectic and Al layers. Both of these can contribute to high stress concentration. The origin of such interfacial features can be appreciated better by understanding the fabrication processes used for these solar cells. Screen printing technique is often used to deposit Ag finger and Al layer on Si in commercial solar cells, wherein both contacts are made simultaneously by "firing" the sample to around 600–850°C.[13,14] During the firing process, Al-Si eutectic and BSF are formed due to diffusion of Al into Si.[15] It is reported that at the end of the firing process, the bulk porous Al layer also consists of some loosely connected Al-Si particles; this is attributed to the rapid diffusion of Si at high temperatures into the Al layer covered with an Al_2O_3 layer.[2,3] Consistently, it has been suggested that particle-to-particle contact in the porous Al layer was made through the thin oxide layer created around them.[2,15] The presence of an oxide layer was also confirmed by the EPMA (not shown here) performed on the test-samples used in this study. Such bonding would be fairly weak, as compared to

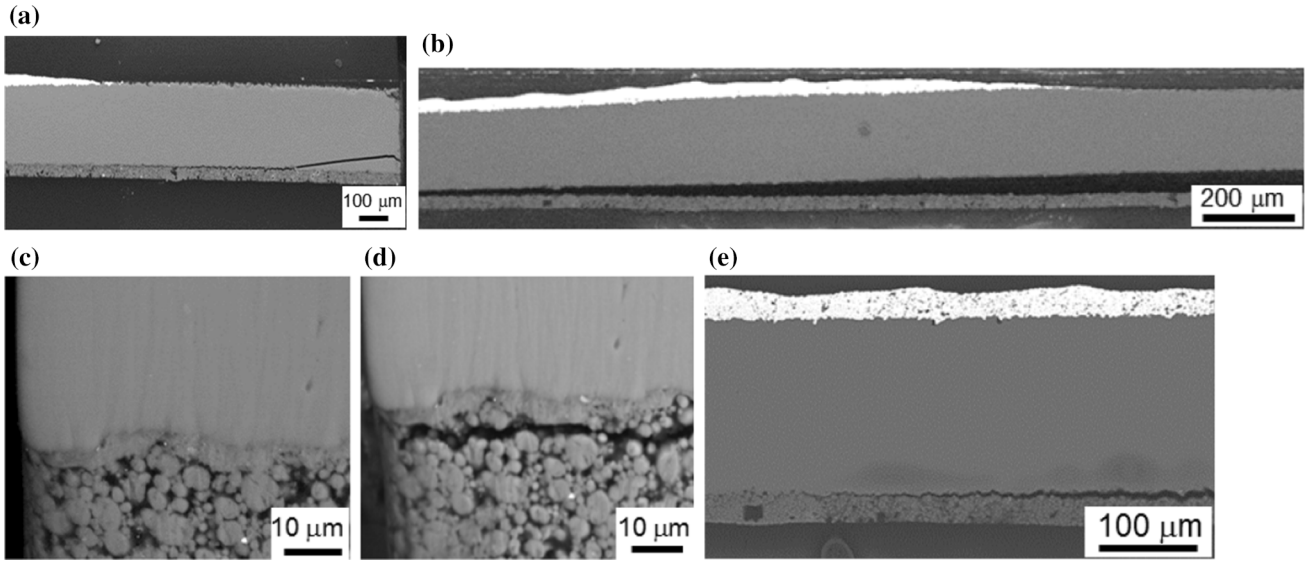

Fig. 6. SEM micrographs showing the cross-section of solar cell near the Al-Si interface: A sample after (a) 1 and (b) 100 thermal cycles, and a metallographically polished sample (c) before, (d) after five thermal cycles and (e) after 100 thermal cycles. Regions shown in (c) and (d) represent the same location before and after thermal cycling. Thermal cycling was performed between − 40°C and 90°C at ramp-rate for heating and cooling of 100°C/h.

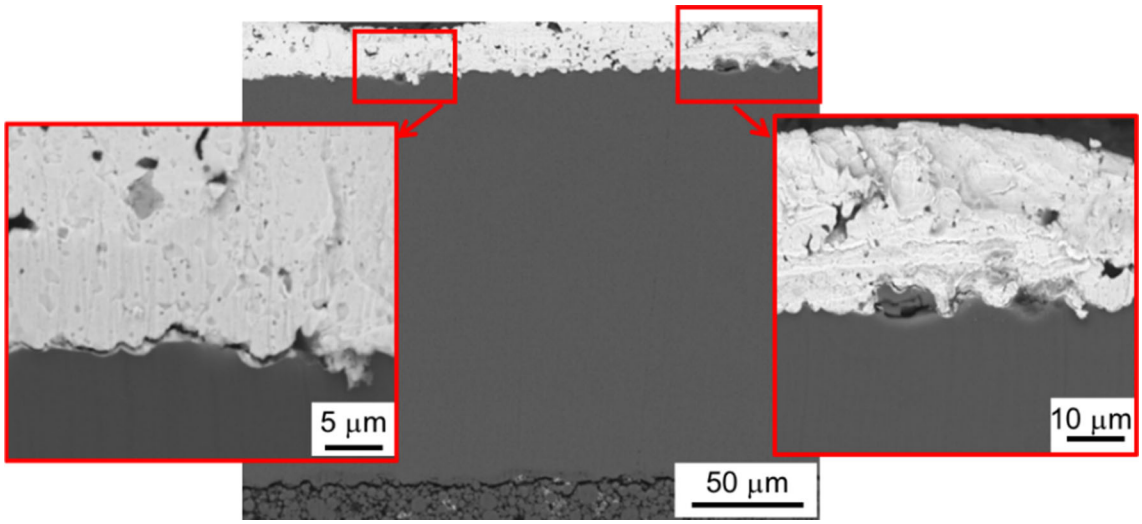

Fig. 7. SEM micrographs, obtained at various magnifications, showing a solar cell sample, especially regions near the Si-Ag interface, after 70 thermal cycles. Thermal cycling was performed between − 40°C and 90°C at ramp-rate for heating and cooling of 100°C/h.

other layers or regions in the solar cell, thereby leading to easy failure of Al-Si eutectic and Al layer interface. It should be noted that composition of Al-Si eutectic did not vary near the interface of Al layer and Si, and therefore it was assumed that properties of Al layer near the interface were not affected due to any composition variation. On the other hand, since Ag layer is screen printed on relatively rough surface of silicon nitride,** its adhesion with Si becomes significantly better than that between Al and Si.[2,16] In addition, the Ag-Si interface remains relatively smooth compared to the Al-Si interface. Therefore, unlike the Al-Si interface, damage did not occur in the Ag layer during the initial cycles. Now, once a crack gets nucleated in the sample due to the cyclic thermal stresses, it can propagate easily through the eutectic-Al interface and Al layer as spherical particles in this layer were weakly bonded. Furthermore, it is also possible that Al-Si eutectic layer, which is fairly ductile and homogenous as compared to the porous Al layer, does not allow the crack to deflect inside it, and hence it

**Silicon nitride surface, which is deposited on top of Si, is often roughened by etching so that it can efficiently trap the solar radiation by reducing reflection.

protects the brittle Si from fracture. Similar observations regarding the delamination behavior of metal layers in Si solar cells have also been reported in 3-point [2] and 4-point [3] bending tests.

Finite Element Analysis

Figure 9 shows variation of the representative elemental normal stresses in the y-direction (i.e., vertical direction, which would lead to interfacial delamination) in each layer of the solar cell with smooth interfaces as function of temperature during the first 10 thermal cycles. When the build-up of these thermal stresses becomes greater than the yield strength of the material at a location, plastic deformation would occur locally. Due to the plastic deformation, the stress–strain profile for this region becomes nonlinear, resulting in not only formation of a stress–strain hysteresis over a thermal cycle, but also a build-up of residual stress, especially in the significantly constrained layers at the end of the thermal cycle; this has been aptly captured in the plots shown in Fig. 9. Furthermore, due to the strain hardening the built-up stresses would continue to increase with number of thermal cycling, resulting in expansion of the plastic zone in the sample and hence the size of the hysteresis loop. Such an increase in the hysteresis loop, along with increase in the maximum stress during subsequent thermal cycling, were observed in Ag and the Al-Si eutectic layer, as shown in Fig. 9a and b, respectively. This clearly suggests an increase in the size of the plastically deforming regions in these layers, which would then lead to an increased resistance to the fracture (or crack propagation) in these metallic layers. It should be noted that the FE simulations performed here did not account for nucleation and growth of cracks, and hence the built-up stresses were relaxed only due to the plastic deformation.

On the other hand, if plastic deformation is negligible in a material, then not only would the size of the stress–strain hysteresis loop be small, but also the residual stress at the end of a thermal cycle would be negligible (i.e., the start and end points of the stress versus temperature curve would coincide with each other). This is likely to occur in a material that is either freely expanding (i.e., without significant constraint from the neighboring differentially expanding components) or deforming dominantly in the elastic fashion. It is possibly the reason why the porous Al layer, which was constrained only at one end and that too by a material layer with similar CTE (i.e., Al-Si eutectic), did not show significant hysteresis (see Fig. 9c). It should be noted that although the extent of the shielding of the mechanical constraint applied by Si on the Al layer due to intermediate Al-Si eutectic layer also depends upon the thickness of the eutectic layer, the constraint applied by Si on Al layer was significantly shielded by the eutectic layer in these samples. However, it is

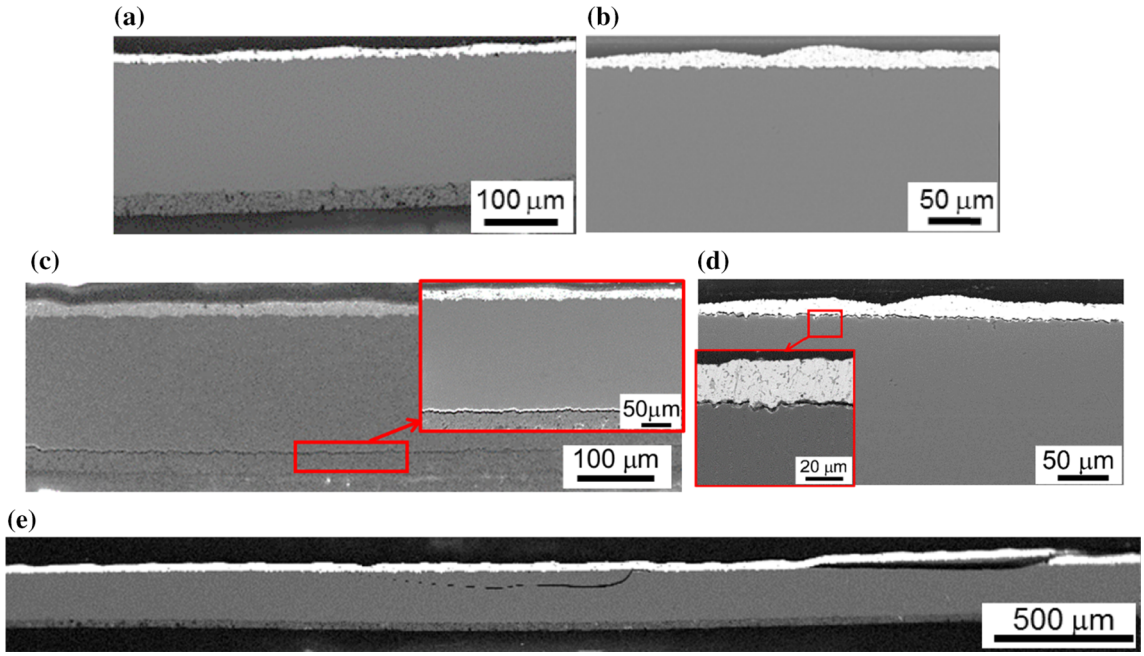

Fig. 8. SEM micrographs showing effect of 10 thermal cycles performed at a faster ramp rate of 230°C/h on structural integrity of a solar cell sample: (a) low magnification micrograph showing entire cross-section of the sample and (b) a slightly higher magnification micrograph showing the region near Si-Ag interface before thermal cycling, and (c) low magnification and high magnification (inset) micrographs focusing on Al-Si interface, (d) low magnification and high magnification (inset) micrographs focusing on Si-Ag interface, and (e) low magnification micrograph showing entire cross-section of the solar cell after thermal cycling.

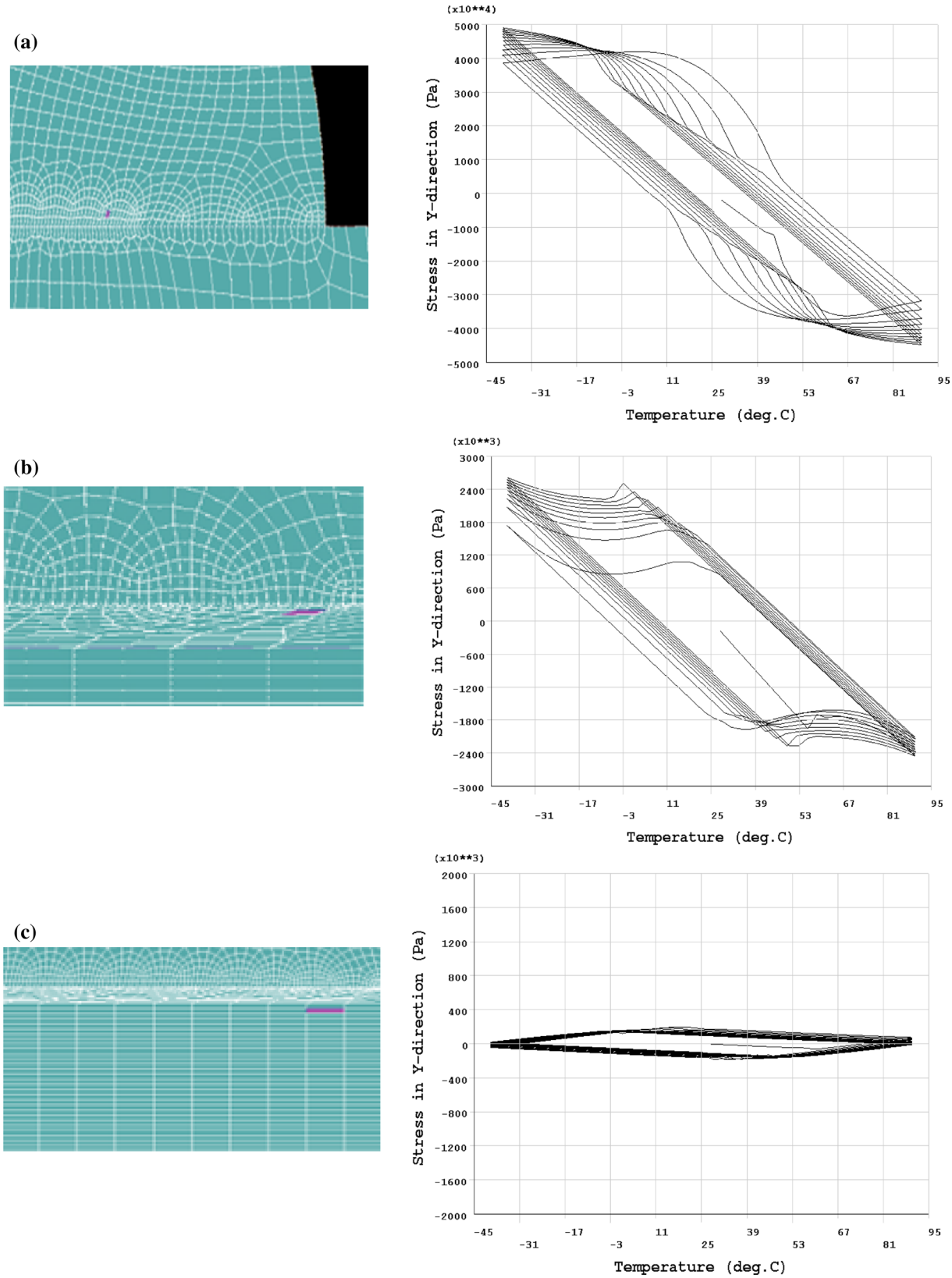

Fig. 9. Variation of σ_{yy} in an element (shown by the pink shade in the FEM model shown in inset on the left) as function of temperature during the first 10 thermal cycles in: (a) the Ag finger close to the Ag-Si interface, (b) the eutectic layer near interface between Si and the Al-Si eutectic layers, and (c) the Al layer near the Al-Si eutectic and the Al interface.

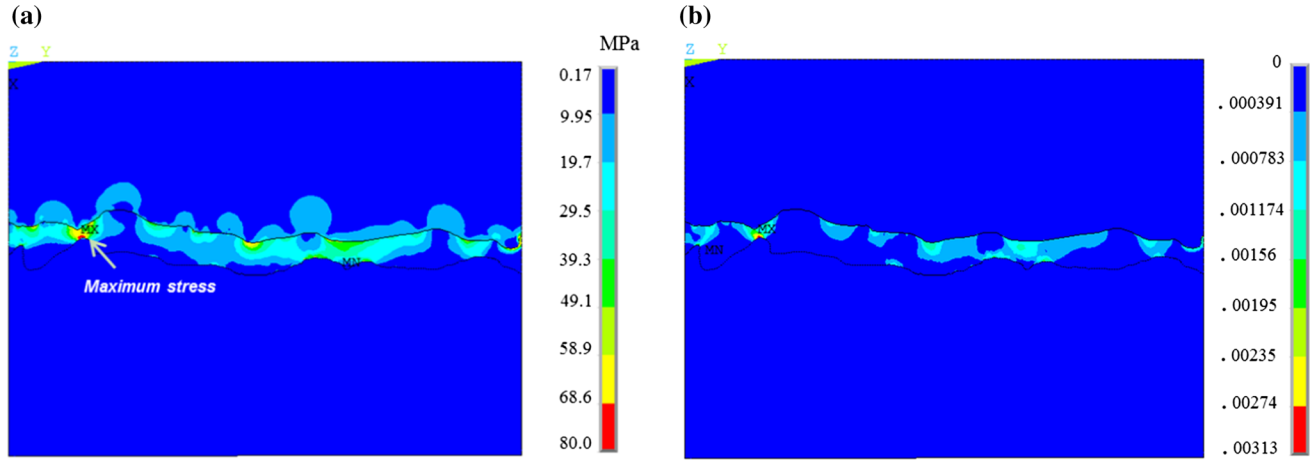

Fig. 10. 2D color contour plots showing distribution of (a) stress intensity (i.e., difference between maximum and minimum principal stresses) and (b) von Mises plastic strain in a microstructurally aware FE model near the Al-Si interface at the end of the first thermal cycle (Color figure online).

expected that this shielding effect will significantly reduce stress built up in the Al layer as compared to that in Ag and Al-Si eutectic layers, which are in direct contact with Si. Accordingly, as shown Fig. 9-c, the value of stress build-up in the Al layer with number of thermal cycles was not significant. However, this is contrary to the experimental observations made in this study, which revealed easy crack propagation in the Al layer, especially near the interface of the Al-Si eutectic and Al layer. This warrants critical evaluation of the effect of roughness of the interface(s) on the stress field, as described next.

The effect of roughness or irregular wavy nature of the interfaces could be easily captured using the microstructurally aware FEM. Figure 10a, which shows the distribution of stress intensity in the region near Al-Si interface after the first thermal cycle, reveals that the highest stress concentration occurred within the eutectic layer. Furthermore, the highly curved regions of the eutectic layer near the Al-Si eutectic and Al layer interface registered the highest stress intensity (of 40-80 MPa). Furthermore, the plastic strain, whose distribution is shown in Fig. 10b, was concentred near the Si-eutectic interface, and hence there will be higher resistance for the crack to grow along this interface. Although the location of the highest value of plastic strain was the same as where stress intensity was maximum (i.e., at bend, Fig. 10a), on average, the magnitude of plastic strain at the Si-eutectic interface was higher than at the Al-eutectic interface. This further confirms that plasticity in the eutectic layer shields Si from crack deflecting into it. Hence, consistent with the experimental observation, Fig. 10 suggests that the crack would nucleate and propagate mostly along the porous Al-eutectic interface, and the fracture of Si layer would not take place.

XFEM Study

XFEM allows understanding of growth of discontinuities, (e.g. cracks), without the need for re-discretizing the model at each iteration. Now, if the crack location in the solar cell model was not defined a priori, then as shown in Figs. 11a and b, micro-cracks nucleated in the Al layer near the interface of the Al-Si eutectic and Al layers in all models, i.e., irrespective of the nature of the interface (i.e., wavy or flat interface geometry). Furthermore, when the damage initiation properties were varied, then it was observed that the cracks did not nucleate if the Al layer's fracture strength was greater than 50 and 35 MPa for the wavy and the smooth interface, respectively. This difference in the crack nucleating fracture strength clearly shows that crack nucleation in a sample with smooth Al-eutectic interface was significantly more difficult. In this context, it should also be noted that although stress in the Si-eutectic-Al system would reduce if plastic deformation occurs in the eutectic (and Al) layer, the curvy locations in the irregular wavy interface will still amplify the stress locally, resulting in facilitation of nucleation of micro-cracks or damages at lower value of the average or far-field stress (see "Finite Element Analysis" section). Hence, attempt should be made to develop processing routes that produce smooth Al-Si interface. It should be noted that a direct comparison of XFEM results with the experimental observation about the precise location of the crack may not be quite possible as XFEM could not predict crack nucleation at the sharp interface between Al and the eutectic layer; however, the insights into the effects of the waviness and the interfacial strength on the ease of crack nucleation in the system as discussed here can be useful.

In order to understand the effect of geometry of the Al-eutectic interface and the fracture strengths

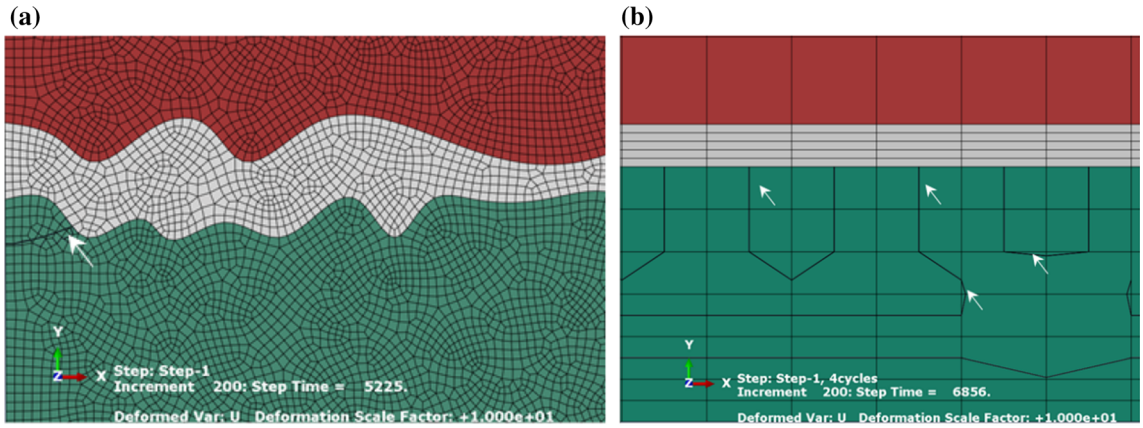

Fig. 11. XFEM results showing crack nucleation in Al in the vicinity of the Al-Si interface when a specific location for the crack nucleation was not defined a priori: Models with (a) wavy irregular interface and (b) smooth interface. Here, the top red, middle grey and bottom green regions represent Si, Al-Si eutectic and Al layer, respectively. The location of crack nucleation in (a) and (b) is shown by an arrow (Color figure online).

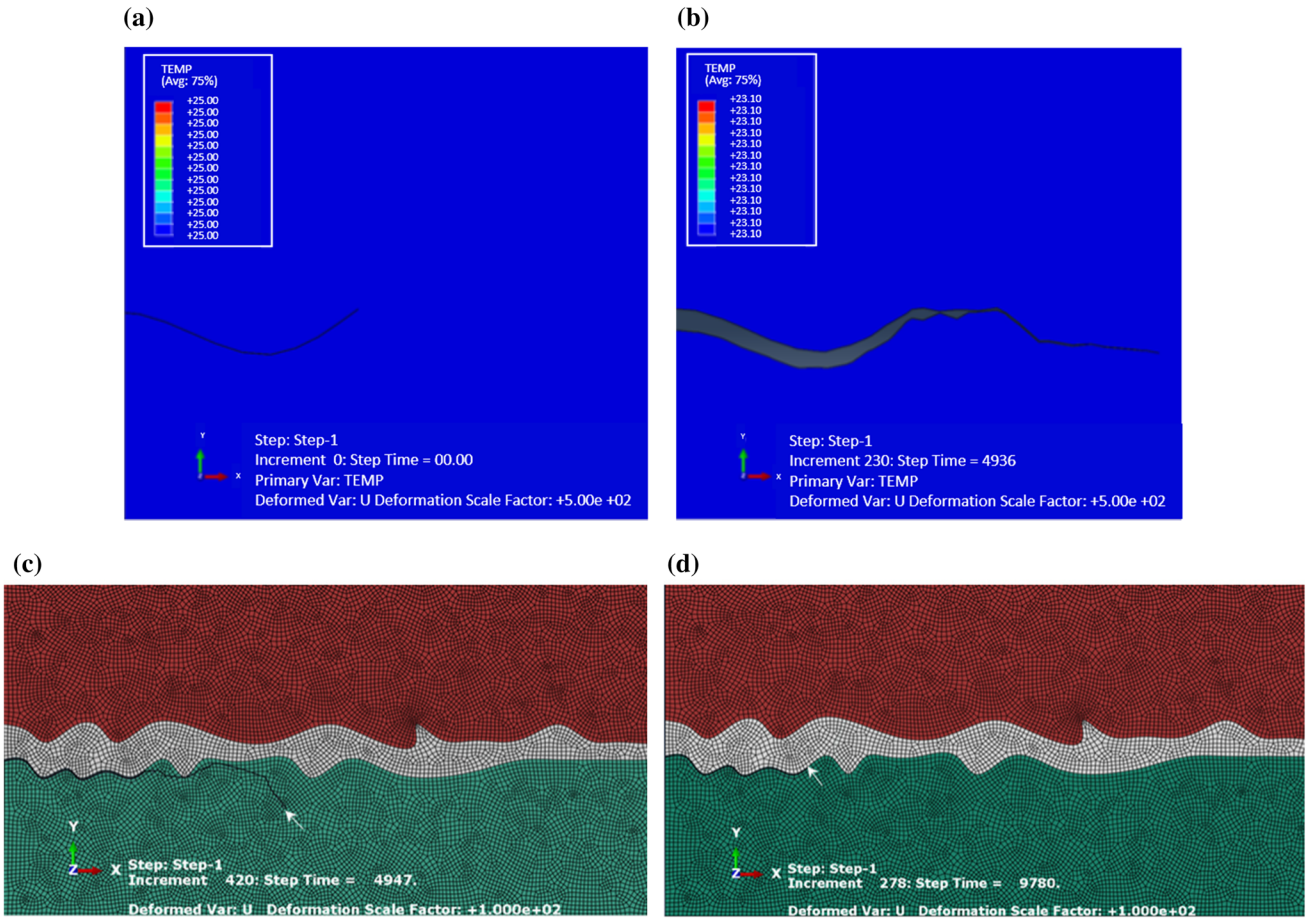

Fig. 12. XFEM results showing propagation of a pre-existing crack in a model with irregular wavy interface due to thermal cycling: (a) Initial configuration, i.e., before applying a thermal load, (b) at the start of the cooling segment of the first thermal cycle (here, interfacial fracture strength was equal to 10 MPa), (c) during subsequent cooling cycle, showing deflection of the crack away from the eutectic-Al interface into Al layer (here also, interfacial fracture strength was equal to 10 MPa), and (d) crack arrest, i.e., its failure to grow, in a sample with very high interfacial fracture strength (of 150 MPa).

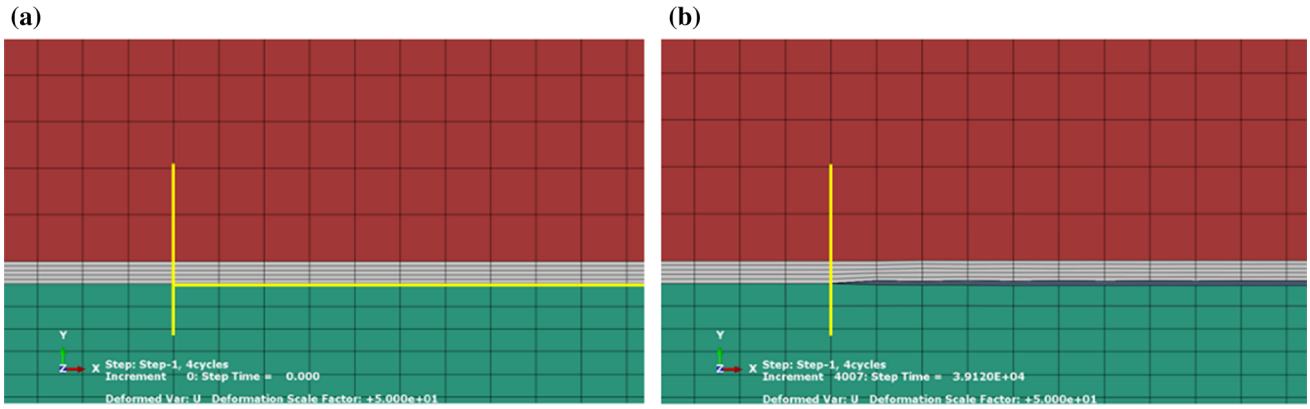

Fig. 13. XFEM results showing effect of thermal cycling on a pre-existing crack in a model with smooth interface: (a) Initial configuration, i.e., before applying a thermal load, and (b) after four thermal cycles (here, crack propagation was not observed). Here, the interfacial fracture strength was low and equal to 10 MPa.

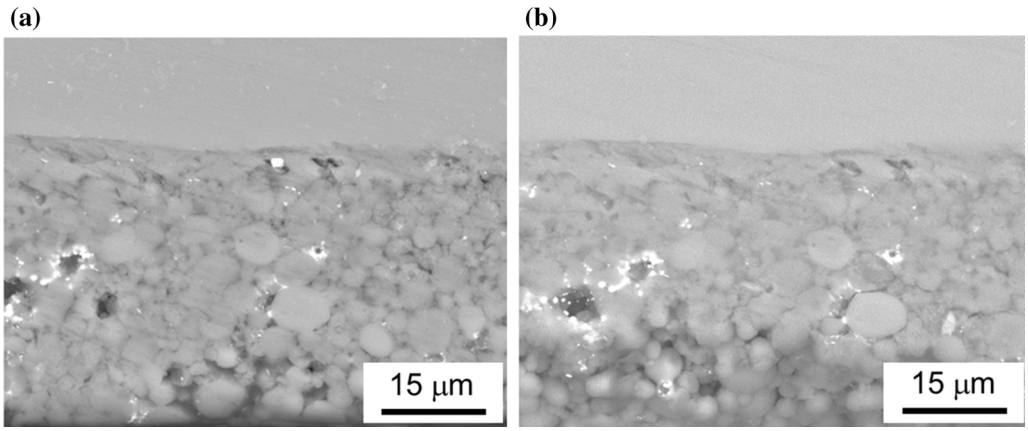

Fig. 14. SEM micrographs showing the cross-section of a solar cell near the Al-Si interface: (a) before, (b) after 55 thermal cycles performed between − 40°C and 90°C. The Al layer in this solar cell was not only relatively less porous, but also formed smoother interface with Al-Si eutectic layer, as compared to the solar cell used for the remainder of this study (see Figs. 1d and 6c). Micro-crack nucleation or any other type of damage nucleation was not observed for these set of samples even after 55 thermal cycles.

of different components on crack growth, XFEM-based simulations were performed using the models with pre-existing cracks along the Al-eutectic interface. Figures 12 and 13 show the simulation results for the models with irregular wavy and the smooth Al-eutectic interfaces, respectively. Figure 12a shows the initial configuration of the crack in the model with irregular wavy interface, and as shown in Fig. 12b, this crack continued to propagate along the same Al-eutectic interface with thermal cycling. Herein, the fracture strength of the Al layer was assigned a low value of 10 MPa. The crack propagation occurred during the cooling segment of the thermal cycle, as therein tensile stresses were generated in Al and eutectic layers (i.e., the layers with CTE higher than that of Si). As a matter of fact, the crack growth shown in Fig. 12b occurred at the onset of the cooling segment of the first cycle itself. Now, as shown in Fig. 12c, the crack was deflected away from the interface towards the Al layer once the crack became longer (i.e., during subsequent thermal cycle) However, this was not observed in the experiments; most likely it would require crack to become very long. Furthermore, XFEM results clearly show that the crack did not deflect towards the interface of the eutectic layer and the Si, thereby confirming the efficacy of the eutectic layer in shielding Si, which is extremely brittle material, from crack propagation and, eventually, fracture. Now, as shown in Fig. 12d, if the fracture strength was increased to a very high value of 150 MPa, then neither the existing interfacial crack propagated, nor any new micro-crack was nucleated in the model. Hence, the XFEM results shown in Figs. 11 and 12 clearly show the important role of the interfacial fracture strength in both crack nucleation and the crack propagation for the case when the interface between Al and Al-Si eutectic was irregular wavy. However, as shown in Fig. 13, the existing crack did not propagate at all after several thermal cycles if the interface was perfectly smooth, even though the assigned fracture strength of the interface was quite low (and equal to 10 MPa). Therefore, it appears that the smoothness

of the interface is the most important factor in determining the structural integrity of the monocrystalline Si solar cells and hence one must tailor the processing parameters to produce smooth Al-eutectic interface (and Al-Si) interface. For example, Fig. 14 shows a solar cell that had smoother eutectic-Al interface, and hence was significantly more resistant to thermal stress induced delamination. In this regard, thin film deposition or electroplating techniques, which are known to produce strong and smooth interfaces, are recommended to be used for depositing Al layer for BSF and back side electrode application.

SUMMARY

Accelerated thermal cycling tests between − 40°C and 90°C were carried out up to 100 cycles on a commercial polymer encapsulated monocrystalline Si solar cell. The samples readily failed by crack nucleation and propagation along the interface of the Al-Si eutectic and Al layers (i.e. backside). Failure along the Ag-Si interface was less likely, and it occurred only when very fast ramp rate for heating and cooling was used.

FE simulations showed that the built-up thermal stresses were high enough to cause plastic deformation in Al, Al-Si eutectic and Ag layers. The irregular wavy geometry of the Al-eutectic interface concentrated stress at this interface, especially at highly curved regions. These stresses were high enough to delaminate the Al layer away from the rest of the solar cell. On the other hand, plasticity in the eutectic layer shielded Si from crack that continued to propagate either along the Al-eutectic interface or inside Al layer.

XFEM results showed relatively easier crack nucleation and crack propagation in the samples with irregular wavy Al-eutectic interface, especially if the fracture strength of this interface was low. Often, the crack nucleated as well as propagated along the Al-eutectic interface, irrespective of the geometry of this interface.

For fabrication of a Si solar cell resistant to the thermal stress induced structural damage, one must select processing techniques that produce very strong and smooth Al-Si interface.

ACKNOWLEDGMENTS

Praveen Kumar would like to thank the Indian National Science Academy (INSA) for financial support for this project under its Young Scientist Research Award Scheme. The authors also thank the Department of Science and Technology (DST), Government of India, for partial financial support (Grant #DSTO 1164). The authors thank Professor Sushobhan Avasthi of the Indian Institute of Science, Bangalore, for providing the samples with smoother interface and fruitful discussions.

REFERENCES

1. Snapshot of Global Photovoltaic Markets; Report IEA PVPS T1-35: 2019. International Energy Agency (IEA): Paris, France (2019), http://iea-pvps.org/index.php?id=266. Accessed 25 Apr 2019.
2. V.A. Popovich, TU Delft. Delft University of Technology (2013).
3. F. Kaule, W. Wang, and S. Schoenfelder, *Sol. Energy Mater. Sol. Cells* 120, 441 (2014).
4. C. Ferrara and D. Philipp, in *International Conference on Materials for Advanced Technologies 2011, Symposium, Energy Procedia*, vol. 15, p. 379 (2012).
5. A. Ndiaye, A. Charki, A. Kobi, M.F. Cheikh, C. Kébé, A. Pape, and V. Sambou, MF, A. *Sol. Energy* 96, 140 (2013).
6. J.H. Wohlgemuth, D.W. Cunningham, A.M. Nguyen, G. Kelly and D. Amin, in *Proceedings of PV Module Reliability Workshop*.
7. J.H. Wohlgemuth and S. Kurtz, in *IEEE International Reliability Physics Symposium Monterey, California*, April 10–14 (2011).
8. A. Skoczek, T. Sample, E.D. Dunlop and H.A. Ossenbrink, *Sol. Energy Mater. Sol. Cells* **92**(12), 1593 (2008).
9. Nick Bosco, Joshua Eafanti, Sarah Kurtz, Jared Tracy, and Reinhold Dauskardt, *IEEE J. Photovolt.* 7, 1536 (2017).
10. O. Hasan, A.F.M. Arif and M.U. Siddiqui, in *ASME 2012 International Mechanical Engineering Congress and Exposition, American Society of Mechanical Engineers*, pp. 495 (2012).
11. S. Wiese, R. Meier, F. Kraemer, J. Bagdahn, EuroSim E., S. Wiese, R. Meier, F. Kraemer and J. Bagdahn, in *10th Proceedings of International Conference on Thermal, Mechanical and Multiphysics Simulation and Experiments in Micro-Electronics and Micro-Systems, EuroSimE, Delft, The Netherlands*, 1 (2009).
12. S. Wiese, F. Kraemer, N. Betzl and D. Wald, in *11th Proceedings of International Conference on Thermal, Mechanical and Multiphysics Simulation and Experiments in Micro-Electronics and Micro-Systems, EuroSimE, Bordeaux, France*, 1 (2010).
13. C. Ballif, D.M. Huljić, G. Willeke and A. Hessler-Wyser, *Appl. Phys. Lett.* **82**(12), 1878 (2003).
14. Mohanmed M. Hilali, Ajeet Rohatgi, and Sally Asher, *IEEE Trans. Electron Devices* 51, 948 (2004).
15. V.A. Popovich, M.P.F.H.L. Van Maris, J. Janssen, I.J. Bennett and I.M. Richardson, *Mater. Sci. Appl.* **4**, 118 (2013).
16. C.-H. Lin, S.-P. Hsu, and W.-C. Hsu, Silicon solar cells: Structural properties of Ag-contacts/Si-substrate.*Solar cells-silicon wafer-based technologies* (Rijeka: IntechOpen, 2011).